American Mineralogist, Volume 91, pages 1150–1162, 2006

Angular dependence of potassium *K*-edge XANES spectra of trioctahedral micas: Significance for the determination of the local structure and electronic behavior of the interlayer site

GIANNANTONIO CIBIN,[1,2] ANNIBALE MOTTANA,[1,2,*] AUGUSTO MARCELLI,[2] AND MARIA FRANCA BRIGATTI[3]

[1]Dipartimento di Scienze Geologiche, Università degli Studi Roma Tre, Italy
[2]Istituto Nazionale di Fisica Nucleare, Laboratori Nazionali di Frascati, Italy
[3]Dipartimento di Scienze della Terra, Università di Modena e Reggio Emilia, Italy

ABSTRACT

The X-ray absorption angle-dependent behavior at the potassium *K*-edge has been determined for two end-members and two intermediate trioctahedral micas, which are representative of the $Fe^{2+}Mg_{-1}$, $Fe^{3+}Al_{-1}$, $SiAl_{-1}FeLi_{-1}$, and $F_{-1}OH$ exchange vectors, using horizontally polarized synchrotron radiation. Experimental spectra are interpreted by the multiple scattering theory following decomposition according to the angular dependence approach of Brouder (1990). The experimental spectra sum up anisotropic effects deriving from in-plane and out-of-plane photoelectron interactions with the potassium near- and next-near neighbors up to the fifth/sixth coordination sphere. For the first time, the absorption edge of a low Z atom is decomposed so as to produce two partial patterns giving, respectively, the full in-plane absorption spectrum ($\sigma_{\parallel}$) and the full out-of-plane spectrum ($\sigma_{\perp}$). They fully describe the complete X-ray absorption dichroic behavior of layered compounds, of which mica is a prototype. $\sigma_{\parallel}$ essentially reflects the arrangement of the atoms located in the mica interlayer space and facing tetrahedral sheets. Differences among the four micas depend on structural changes induced by the adaptation of their tetrahedral sheets to the increasing sizes of their octahedral sheet due to chemical substitutions (i.e., the $Fe^{2+}Mg_{-1}$ vector, mainly) and to chemical changes at the octahedral anion site ($F_{-1}OH$ vector). By contrast, $\sigma_{\perp}$ reflects multiple-scattering interactions entering deep into the mica structure, beyond the tetrahedral sheet and well into the octahedral sheet. Such contributions reflect both changes in the anions coordinating the octahedral cations and increasing total amount of heavy atoms (essentially Fe), and differ based on electronic properties such as oxidation states (e.g., Fe^{2+} and Fe^{3+}). Therefore, angle-dependent XANES spectroscopy is one of the rare spectroscopic techniques able not only to detect, but also to quantify structural effects in the atoms at the medium- to long-range order.

Keywords: Mica, XAS, polarized XANES, potassium *K*-edge, trioctahedral micas, crystal structure

INTRODUCTION

Many studies have been devoted to the definition of structure and layer topology in micas. An overview of the theoretical and experimental knowledge so far acquired may be attained from numerous reviews (e.g., Mottana et al. 2002b; Fleet 2003). Despite this work, mostly based on single-crystal X-ray diffraction (SC-XRD) techniques, many structural and crystal chemical aspects still require further investigation by complementary methods, such as spectroscopy.

The general formula of the mica group of phyllosilicates (cf. Rieder et al. 1998) can be written as:

$$A\ M_{2-3}\ \square_{1-0}\ T_4\ O_{10}\ W_2$$

where

A = K, Na, Ca, Cs, NH_4, Rb, Ba, … is the interlayer cation;

M = Mg, Fe, Al, Ti, Li, Mn, Zn, Cr, V, … is the octahedral cation, which is located in a trioctahedral site when divalent and in a dioctahedral one when trivalent, □ being the vacant site in the latter sheet;

T = Si, Al, Fe, Be, B, … is the tetrahedral cation; and

W = OH, F, Cl, O, and S … is the anion located at the O4 site of the octahedral sheet.

Starting from the formula of phlogopite, $KMg_3[OH_2|AlSi_3O_{10}]$ – *C*2/*m*, the trioctahedral mica prototype end-member, all other trioctahedral end-members are easily derived by using appropriate exchange vectors; e.g., annite by the $Fe^{2+}Mg_{-1}$ exchange vector, which affects the octahedral sheet only, tetra-ferriphlogopite by the $Fe^{3+}Al_{-1}$ vector affecting the tetrahedral sheet, etc. Consequently, deriving solid solution series is greatly simplified, e.g., the phlogopite-annite viz. biotite series (Rieder et al. 1998).

The topology and the crystal chemical role of the interlayer cation *A* were discussed by many authors (e.g., Brigatti and

* E-mail: mottana@uniroma3.it

Guggenheim 2002), particularly in terms of the constraints imposed by its structural confinement between two tetrahedral sheets. Originally, Pauling (1930) conceived a structural model for idealized and undeformed micas in which he suggested 12-fold coordination for the *A* cation and, consequently, implied *P*(6/*m*)*mm* planar symmetry for the interlayer (Smyth and Bish 1988). However, Belov (1949) and later Radoslovich (1961) and Radoslovich and Norrish (1962) recognized an alternative ditrigonal structural model, where the *A* cation has 6 oxygen near neighbors (NN) and 6 oxygen next-nearest neighbors (NNN) in two different configurations having $P(\bar{3})1m$ and $P(\bar{6})2m$ planar symmetry, respectively (Nespolo et al. 1997). In both configurations the effective coordination number (ECoN), i.e., the number of neighbors around the *A* cation that are actually linked to it by bonds of nearly equal length and force (Hoppe 1979; Hoppe et al. 1989; Nespolo et al. 1999), is the same. Weiss et al. (1992) calculated ECoN of the interlayer cation in micas based on Hoppe's equation. They found ECoN to be close to 12 in tainiolite and annite (nomenclature after Rieder et al. 1998), to vary from 11 to 9 in polylithionite, ferroan polylithionite, phlogopite, and ferroan phlogopite, to range between 9 and 8 in dioctahedral true micas muscovite and celadonitic muscovite and, finally, to reach 6 in the dioctahedral true mica paragonite and in most brittle micas. Thus, the coordination of the interlayer *A* cation appeared to be inversely related to the tetrahedral rotation angle α, a result later confirmed and extended by Brigatti and Guggenheim (2002) on the basis of a wide systematic survey of the crystal chemical literature. Furthermore, the coordination of the interlayer *A* cation was found to depend on the polytype (Backhaus and Ďurovič 1984; Nespolo et al. 1997; Nespolo and Ďurovič 2002) and to be affected by the interlayer separation, which from a crystal chemical viewpoint mostly mirrors chemical substitutions affecting the cationic and anionic octahedral sites (Brigatti and Guggenheim 2002).

The interplay between interlayer and tetrahedral sites is also associated with distortion of each tetrahedron and of the entire tetrahedral sheet. Parameters τ (tetrahedral flattening angle) and Δz (basal tetrahedral oxygen plane corrugation) are commonly used to describe the tetrahedron and tetrahedral sheet distortions, respectively. With respect to the ideal value of 109.47° of an undistorted tetrahedron, the τ value increases with the Si atom content of the mica and with the increase in distance between the tetrahedral cation and the basal oxygen plane (alternatively, as the distance between tetrahedral basal O atoms decreases), thus reflecting a dimensional adjustment between tetrahedral and octahedral sheets (Brigatti and Guggenheim 2002). The parameter Δz mostly reflects differences in distance between apical O atoms linked to octahedra of different size (Lee and Guggenheim 1981). Thus, the interlayer *A* cation is closely affected not only by the atomic displacements occurring in the adjacent tetrahedral sheets, but also by those occurring in the octahedral sheet, also for what concerns the anionic sites of the *M* octahedra, i.e., *W*. Indeed, in addition to the four oxygen atoms shared with the tetrahedra, two *W* anions coordinate the octahedral cation: most commonly OH, but also F, Cl, and even O^{2-}. They may be located in a *trans*- viz. *cis*-orientation with respect to the cation, thus inducing different interactions. These interactions still need further explanation and appear to be mostly related not only to the effective coordination number of the *A* cation, but also to short-range order (SRO) configurations. We are currently studying these questions using X-ray absorption near-edge structure (XANES) spectroscopy, a synchrotron radiation (SR) based spectroscopic technique that is acknowledged to be most effective for local studies where an atom oxidation state, coordination, and site distortion (i.e., bond lengths and angles) are involved.

In the past we used X-ray absorption fine structure (XAFS) spectroscopy to investigate the local behavior of Al, Si, Mg, Cr, Fe, and K and the ordering configurations of trioctahedral micas within the theoretical framework of the multiple-scattering (MS) theory (Natoli et al. 2003; cf. Mottana 2004 for a description) using powders as study materials (Mottana et al. 1997, 2002a; Brigatti et al. 2001; Giuli et al. 2001; Tombolini et al. 2002a, 2002b; Cardelli et al. 2003; Wu et al. 2003, 2005; Cibin et al. 2005). In the present work, single crystals rather than powders are used to revisit this problem for K, which is the most common interlayer *A* cation in micas (indeed, often loosely called their "alkali" cation), and always in the same multiple-scattering theoretical framework. Potassium was rarely studied by XAFS, possibly because it absorbs in an energy window hardly optimized at most SR facilities. However, it was studied using various theoretical approaches and calculation methods (e.g., Vedrinskii et al. 1982; Lavrentyev et al. 1999; Gomilšek et al. 2001). Being a major constituent, K cannot be disregarded when studying micas. Moreover, mica cleavage flakes, which parallel the interlayer atom structural planes, allow one to use XAFS angular dependence.

Angle-dependent X-ray absorption spectroscopy (AXAS, according to the acronym proposed by Brouder 1990) has already been used to study many Fe- or other transition-metal-bearing compounds, in particular polymers (e.g., Heald and Stern 1977) and layered compounds, first as single crystals (e.g., Brümmer et al. 1971; Stärke et al. 1972; Brown et al. 1977; Dräger et al. 1988; Manceau et al. 1988, 1990; Heumann et al. 1997; Dyar et al. 2001, 2002a, 2002b), then as fine-grained oriented powders (e.g., Manceau et al. 1998, 1999; Manceau and Schlegel 2001). Although this method takes advantage of the polarization properties of synchrotron radiation, it has seldom been applied in mineral studies (Waychunas and Brown 1990), and, in particular, previous AXAS studies on the micas are exceedingly rare (Manceau et al. 1988, 1990; Dyar et al. 2001, 2002a; Mottana et al. 2002a; Tombolini et al. 2003). To the best of our knowledge, these studies never addressed the *A* cation.

Samples and experimental methods

Table 1 lists the trioctahedral micas we used with their chemical data. Table 2 summarizes their structural data relevant to this study. The sample set consists of four trioctahedral micas chosen from a much larger set of samples (cf. Tombolini et al. 2002b; Cibin et al. 2005). They occur as large undeformed flakes with K as the predominant *A* cation (>90 at%). Two samples are close to end-member composition, respectively phlogopite (sample phl-Fr) and tetra-ferriphlogopite (Tas22-1); the other two are intermediate members of the phlogopite–annite (Tag15-3) and polylithionite–siderophyllite (no. 47) solid solution series, respectively. Thus, our micas represent members of exchange vectors $Fe^{2+}Mg_{-1}$, $Fe^{3+}Al_{-1}$, and $SiAl_{-1}FeLi_{-1}$. The first exchange concerns the octahedral sheet only, the second the tetrahedral sheet, and the third both sheets together. The OHF_{-1} anionic exchange vector is also represented in samples phl-Fr and no. 47. Although this substitution is limited to the octahedral sheet, it may affect the interlayer cation multiple-scattering interactions. Taken together, all these substitutions account for most chemical and geometric

TABLE 1. Chemical analyses (oxide wt%) and formulae (apfu) for trioctahedral micas

	phl-Fr	no. 47	Tas22-1	Tag15-3		phl-Fr	no. 47	Tas22-1	Tag15-3
	Weight percentages					Unit-cell content on the basis of $O_{12-x-y}(OH)_xF_y$			
SiO_2	43.38	38.81	41.47	37.41	$^{[iv]}$Si	3.12	3.06	3.11	2.74
TiO_2	0.20	1.72	0.23	2.38	$^{[iv]}$Al	0.88	0.94	–	1.15
Al_2O_3	11.23	18.88	b.d.t.	13.33	$^{[iv]}Fe^{3+}$	–	–	0.89	0.11
Fe_2O_3	b.d.t.	1.58	16.70	6.35	$^{[vi]}$Al	0.08	0.81	–	–
FeO	0.89	21.17	2.74	5.50	$^{[vi]}$Ti	0.01	0.10	0.01	0.13
MgO	26.58	0.30	24.17	20.01	$^{[vi]}Fe^{3+}$	–	0.09	0.05	0.25
MnO	b.d.t.	1.18	0.06	0.13	$^{[vi]}Fe^{2+}$	0.05	1.40	0.17	0.34
ZnO	b.d.t.	0.29	b.d.t.	b.d.t.	$^{[vi]}$Mg	2.85	0.04	2.70	2.19
BaO	b.d.t.	b.d.t.	0.07	0.95	$^{[vi]}$Mn	–	0.08	–	0.01
Li_2O	b.d.t.	1.29	b.d.t.	b.d.t.	$^{[vi]}$Zn	–	0.02	–	–
Na_2O	0.08	0.09	0.05	b.d.t.	$^{[vi]}$Li	–	0.41	–	–
K_2O	10.85	9.80	10.37	9.81	Ba	–	–	–	0.02
H_2O	0.95	0.54	3.55	3.90	Na	0.01	0.01	0.01	–
F	5.75	4.33	0.61	0.22	K	1.00	0.99	0.99	0.92
Cl	0.09	b.d.t.	b.d.t.	b.d.t.	OH	0.46	0.28	1.78	1.91
Sum	100.00	99.98	100.02	99.99	F	1.31	1.08	0.14	0.05
					Cl	0.01	–	–	–
					O	10.22	10.64	10.08	10.04

Notes: Localities: phl-Fr = Franklin, New Jersey; Tag15-3 = Tapira, Minas Gerais, Brazil; no. 47 = Lake George ring complex, Pikes Peak, Colorado; Tas22-1 = Tapira, Minas Gerais, Brazil.
b.d.t. = below detection threshold; dash (–) = below 0.005.

variability in the *TMT* layer of the mica module of the trioctahedral subgroup of micas (Ferraris and Ivaldi 2002; Brigatti and Guggenheim 2002). The symmetry of the *TMT* layer is *C*2/*m* for all micas with the exception of no. 47, which is *C*2 (Brigatti et al. 2000). Thus, no. 47 has three independent octahedra *M*1, *M*2, and *M*3, and layer symmetry *C*12(1), whereas the other trioctahedral micas have only two independent octahedra (*M*2 and *M*3 are symmetry-equivalent), and layer symmetry *C*12/*m*(1).

All samples were tested for chemical homogeneity by carrying out major element analyses on a large number of grains using a WDS ARL-SEMQ electron microprobe (operating condition: 15 kV accelerating voltage, 15 nA sample current and defocused electron beam with about 3 μm spot size). Intragranular compositional variation was within 3% of the estimated standard error, indicating a high degree of chemical homogeneity. Therefore all point data were averaged. Formulae in Table 1 are based on $O_{12-(x+y+z)}$ (where x is OH^-, y is F^-, and z is Cl^-) and were obtained by combining the results of: (1) EMP analysis, as mentioned before; (2) OH^- determination by thermo-gravimetric analysis, using a Seiko SSC 5200 thermal analyzer equipped with the quadrupole mass spectrometer ESS, GeneSys Quadstar 422 to analyze the gases evolved in the thermal reactions. Experiments were carried out in a flow of Ar gas to minimize the reaction $2FeO + 2(OH) \rightarrow Fe_2O_3 + H_2 + O^{2-}$; (3) Fe^{3+} chemical determination by a semimicro volumetric method (Meyrowitz 1970). Lithium was determined by inductively coupled plasma atomic-emission spectrometry (ICP-AES, Varian Liberty 200) on 25 mg aliquots digested in a microwave oven with a mixture of HF and HNO_3 in closed Teflon crucibles.

All samples were also characterized for their long-range order (LRO) structure by single-crystal X-ray diffraction (SC-XRD) refinement. Data collection (using a Siemens P4P rotating-anode single-crystal diffractometer) and structure refinement, in the space groups *C*2/*m* (samples phl-Fr, Tas22-1, and Tag15-3) and *C*2 (no. 47) were carried out according to well-tested procedures described elsewhere (Brigatti et al. 1996, 2000). Appropriate fully ionized scattering factors were applied to the *A*, *M*1, and *M*2 sites, whereas mixed scattering factors were assumed for *T* cations as well as for O and *W* anions. Table 2 reports the structural data relevant to the interpretation of the polarized K-XANES spectra. The complete set of structural data is published elsewhere for samples Tas22-1, Tag15-4, and no. 47 (Brigatti et al. 1996, 2000), and is available on request for phl-Fr.

Angle-dependent XAFS experiments were performed at Stanford Synchrotron Radiation Laboratory (SSRL) with SPEAR2, the storage ring, operating at 3 GeV with current decreasing from 90 to 60 mA. *K*-edge spectra were recorded at beam line SB3-3 with the JUMBO monochromator equipped with InSb crystals cut along the (111) plane, giving a better than 1.5 eV resolution. This results from a 0.9 eV value for the full width at half maximum (FWHM) of the rocking curve (Hussain et al. 1982) plus a calculated 0.41 eV Darwin width for the divergence of the incident synchrotron radiation beam (Lytle et al. 1984). Mica blades or cleavage flakes ca. 10×5×0.3 mm in size were fastened flat onto a vertical Ag-coated sample holder, which could be rotated up to a maximum θ ca. 75–80° from the impinging horizontally polarized synchrotron radiation beam (Fig. 1). Spectra were recorded stepwise at room temperature under high vacuum (ca. 10^{-7} mbar because of the use of channeltrons) for 3–5 s at each 0.5 eV point. We made use of the total electron yield (TEY) detection mode, which probes only few atomic layers closest to surface at the K *K*-edge energy even when the beam impinges the sample at 0° angle (ca. 5 nm: Kasrai et al. 1996). Such a limited electron escape depth warrants the direct proportionality of the TEY signal to the absorption coefficient even at grazing incidence angles (Eisebitt et al. 1993). Consequently, the quality of the sample surface was found to influence significantly the signal to noise ratio (S/N), producing noisy spectra particularly at the highest rotation angles. Unfortunately, this well-known problem (Kasrai et al. 1998) cannot be circumvented in natural materials such as our micas, but only somewhat reduced by smoothing the raw data, taking care that smoothing is never so advanced as to cut information down. The raw spectra were background-subtracted using standard Victoreen polynomials and normalized to ca. 50–60 eV above threshold (Bianconi 1988; Mottana 2004). Energy positions were located as the minima of the second derivative pattern and are accurate ±0.3 eV close to the absorption edge, their inaccuracy increasing

TABLE 2. Data derived from crystal structure refinement of relevance for the interpretation of polarized *K*-XANES spectra

		phl-Fr	no. 47	Tas22-1	Tag15-3
Space group		*C*2/*m*	*C*2	*C*2/*m*	*C*2/*m*
Unit-cell parameters	*a* (Å)	5.309(1)	5.339(1)	5.357(1)	5.329(2)
	b (Å)				
	c	9.198(1)	9.233(1)	9.270(1)	9.228(2)
	c (Å)	10.150(1)	10.135(2)	10.319(2)	10.258(3)
	β (°)	100.08(1)	100.73(1)	99.96(1)	100.03(3)
Tetrahedral parameters	⟨T1-O⟩ (Å)	1.650(2)	1.658(4)	1.670(3)	1.658(3)
	⟨T2-O⟩ (Å)		1.637(4)		
	α (°)	6.7	3.4	10.8	8.5
	thickness (Å)	2.270	2.241	2.254	2.252
	Δ*z* (Å)	0.002	0.058	0.002	0.001
Octahedral parameters	⟨M1-O⟩ (Å)	2.061(2)	2.126(3)	2.088(4)	2.085(4)
	⟨M2-O⟩ (Å)	2.062(2)	2.017(4)	2.089(3)	2.079(4)
	⟨M3-O⟩ (Å)		2.085(4)		
	thickness (Å)	2.111	2.138	2.168	2.167
Interlayer parameters	K-O1	2.982(3)	3.066(1)	2.947(6)	2.983(5)
	K-O1′	3.297(3)	3.256(2)	3.456(6)	3.360(6)
	K-O2	2.988(2)	3.069(4)	2.955(4)	2.974(4)
	K-O2′	3.289(2)	3.237(4)	3.441(4)	3.368(3)
	K-O22		3.075(4)		
	K-O22′		3.180(4)		
	$\langle K\text{-}O\rangle_{inner}$ (Å)	2.986(2)	3.070(4)	2.952(4)	2.977(4)
	$\langle K\text{-}O\rangle_{outer}$ (Å)	3.292(2)	3.224(4)	3.446(4)	3.365(4)
	⟨K-O4⟩ (Å)	4.013(2)	4.062(3)	4.171(3)	4.128(4)
	⟨K-K⟩′ (Å)	5.310(1)	5.333(2)	5.353(2)	5.328(2)
	⟨K-K⟩′ (Å)	5.309(1)	5.339(1)	5.357(1)	5.329(2)
	separation (Å)	3.343	3.339	3.487	3.431

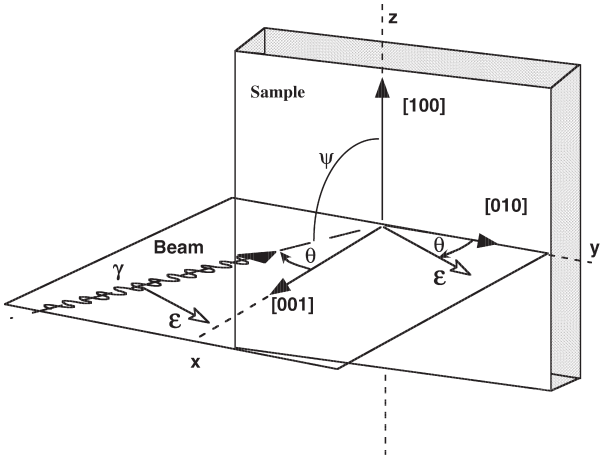

FIGURE 1. Geometrical setting of the mica blades used to record angle-dependent XANES spectra. Blades are secured to the sample holder so as to lie always parallel to its surface. The horizontally polarized synchrotron radiation beam γ of energy *h*ν impinges the blade forming a 90° angle to the vertical direction (ψ) and 0° in the horizontal one (θ). The blade is then rotated on Z by θ, this being the rotation angle between the electric field vector ε and the plane of the sample holder, where the mica Z and Y axes lie.

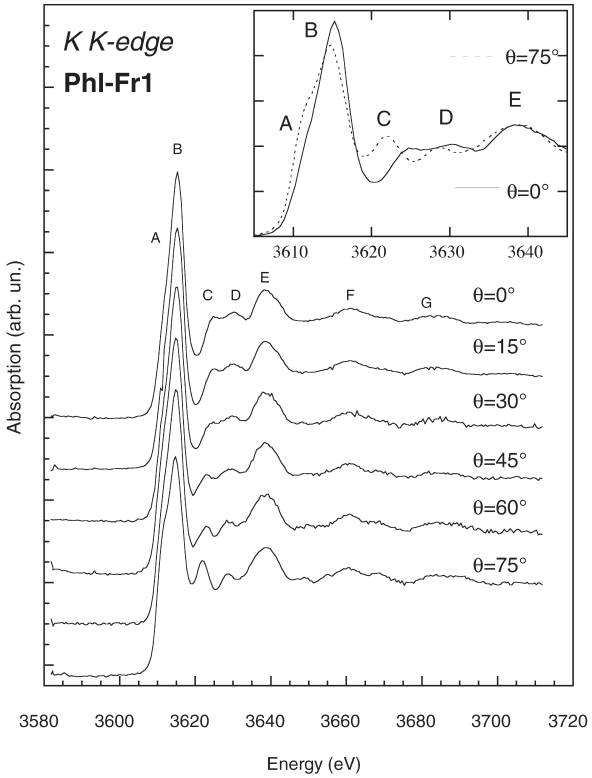

FIGURE 2. Angle-dependent K *K*-XANES spectra recorded on fluorophlogopite phl-Fr (Franklin, New Jersey, U.S.A.) at various θ angles (inset: enlargement of the FMS to IMS section for two extreme rotations).

upwards to ± 1 eV owing to the increased broadness of the features. Intensities (in arbitrary units) are reproducible to ±5 rel.%, their reproducibility again being best next to the edge. Energy calibration was made with reference to K *K*-edge spectra of synthetic KCl (sylvite) repeatedly taken at regular times. The spectrum of this compound was recorded by several experimentalists (e.g., Trischka 1945; Prešeren et al. 1999; Cibin et al. 2005) and also calculated ab initio by a variety of approaches (see above). Thus, its first peak absorption energy, determined as the minimum in the first derivative pattern, has been located at 3611.9 eV (cf. Gomilšek et al. 2001). Natural leucite, microcline, and sanidine, all calibrated against sylvite, were also used as secondary standards.

EXPERIMENTAL RESULTS

Our micas are members of the phlogopite–annite and polylithionite–siderophyllite joins. Their crystal structures were recently refined and discussed in detail by Brigatti and Guggenheim (2002). In particular, tetra-ferriphlogopite (Tas22-1) has been studied for both its average structure (Brigatti et al. 1996) and for its local structure (Giuli et al. 2001). Thus, their atom LRO and ensuing polarization behavior may be considered to be representative for a larger number of trioctahedral micas. Furthermore, their local SRO properties may be understood to be characteristic for most, if not all, trioctahedral micas.

Figure 2 shows the angle-dependent K *K*-edge spectra recorded for phl-Fr, our mica closest to the phlogopite end-member in both its Fe/Σ*M* and K/Σ*A* cation ratios (Table 1), but actually a fluorophlogopite (F/Σ*W* = 0.74; Rieder et al. 1998). The spectra obtained by rotating the blade in θ by 15° steps up to 75° do not change substantially. Seven features can always be seen in the energy range 3600–3680 eV, i.e., in the XANES region of the XAFS spectrum, plus two/three more features at higher energy (not shown) that are related to single-scattering oscillations i.e., to EXAFS (Mottana 2004; Natoli et al. 2003). The XANES region consists of two sub-regions: the full multiple-scattering (FMS) sub-region from the absorption threshold to ca. 3620 eV, and the intermediate multiple-scattering (IMS) sub-region at higher energy. The first 40 eV above threshold are the most interesting part of the spectrum because they show the largest variations on rotation. They contain two features, A and B (notation after Cibin et al. 2005; B being the edge-top), the energy and intensity of which are substantially unchanged upon rotation. This is also the case with feature E, which is the most intense feature in the IMS sub-region. By contrast, all other features, and especially feature C at ca. 3625 eV (cf. Table 3a), undergo significant changes. This last feature is very weak and almost unresolved in the spectrum taken at θ = 0° (i.e., with the synchrotron beam impinging orthogonally onto the mica blade; Fig. 1). It becomes more resolved with no change in energy in the θ = 15° spectrum. However, as the sample is rotated, feature C moves to lower energies with an increase in resolution. In the θ = 75° spectrum feature C is still a minor peak (when compared, e.g., to B), but it appears to be fairly strong and well resolved at 3622.8 eV i.e., at an energy ca. 3.2 eV lower than its initial value. Such an energy move is made conspicuous by the fact that C now falls in the dip in the spectrum following edge-top B that marks the transition from the FMS to the IMS sub-region (Fig. 2, inset). In addition, at θ = 75° the last sub-region shows at least two other very weak and yet resolved and detectable features at ca. 3649 and 3669 eV (Fig. 2, lowest spectrum). Since these two features (and C too) belong to the IMS sub-region, they are primarily structural in origin (Mottana 2004, p. 381; cf. Benfatto et al. 1986). The behavior of C , and that of G, a feature that is

so far away from threshold as to probably belong to the EXAFS region, may be studied in greater detail and with deeper insight using geometrical fitting codes based on the MS theory such as MXAN (Benfatto et al. 2001), as we have recently done with a Cr-bearing muscovite (Cardelli et al. 2003). We plan to carry out these calculations, but we confidently anticipate that by using the XANES angle-dependent properties and appropriate fitting methods one gathers enough quantitative information on the full structural environment around the probed atom.

Figure 3 shows the XAFS angular behavior of Tas22-1, the mica that approaches best the tetra-ferriphlogopite end-member (Brigatti and Guggenheim 2002; Table 1a, n. 33). Its angular behavior is similar to that just seen for fluorophlogopite (Fig. 2), but with some notable differences. Despite the increase of the background noise induced by rotation, it is quite clear that edge-top B suddenly drops in intensity in the final $\theta = 60°$ spectrum (the $\theta = 75°$ spectrum is not shown because it could not be proficiently recorded owing to the noise). Two additional features develop on both its limbs (Fig. 3, inset), i.e., a shoulder on its low-energy side that matches and enhances the A feature seen in previous spectra, and another shoulder (B*) on the high-energy side, not to be seen in the $\theta = 15°$ and 30° spectra but as a faint trace, which cannot be measured. Therefore, sample rotation appears to enhance new MS interactions, which may be of either electronic or structural origin because they occur in the FMS sub-region (Benfatto et al. 1986; cf. Gomilšek et al. 2001). Were they only structural in origin, they would indicate very long MS pathways. Furthermore, feature C decreases in intensity on rotation, but this decrease is only apparent. In fact, it is related to the overlap of C and the newly formed feature B* as C moves to lower energy. The observed movement involves the entire IMS sub-region, and in particular feature F. By contrast, feature G, although difficult to perceive because of the background noise, does not move in energy, thus confirming that it either is an EXAFS-like contribution or it definitively belongs to the EXAFS region (cf. Giuli et al. 2001 for similar features at the Fe *K*-edge of this mica). Consequently, the behavior of feature G confirms that the most local environment directly surrounding the K atom is unaffected by rotation. Implicitly, by comparing the behaviors of G and B* (viz. C) one opens the way to a quantitative evaluation of the photoelectron pathways throughout the mica structure (see below).

Figure 4 shows the XANES spectra obtained by rotating sample no. 47 (a lithian fluorosiderophyllite with $Fe_{tot}/\Sigma M = 0.51$ and $F/\Sigma W = 0.79$: Brigatti and Guggenheim 2002; Table 1b, n. 126; cf. Rieder et al. 1998). All spectra are characterized by a low signal to noise ratio, which decreases with increasing θ. Because of the high noise level, the $\theta = 75°$ spectrum is not shown. Nevertheless, the angular behavior of no. 47 is consistent with those recorded for phl-Fr and Tas22-1, i.e., the FMS features do not move in energy, but they become slightly

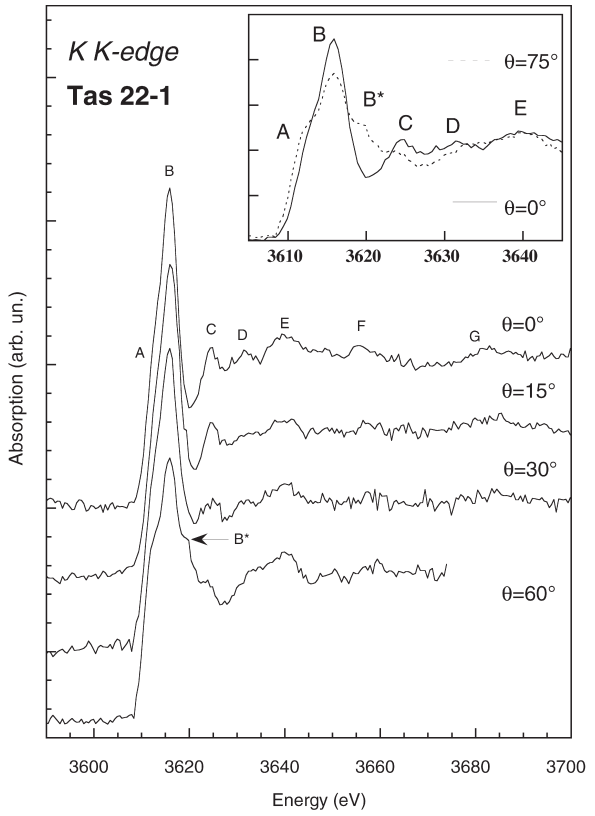

FIGURE 3. Angle-dependent K *K*-XANES spectra recorded on tetra-ferriphlogopite Tas22-1 (Tapira, Minas Gerais, Brazil) at various θ angles (inset: enlargement of the FMS to IMS section for two extreme rotations).

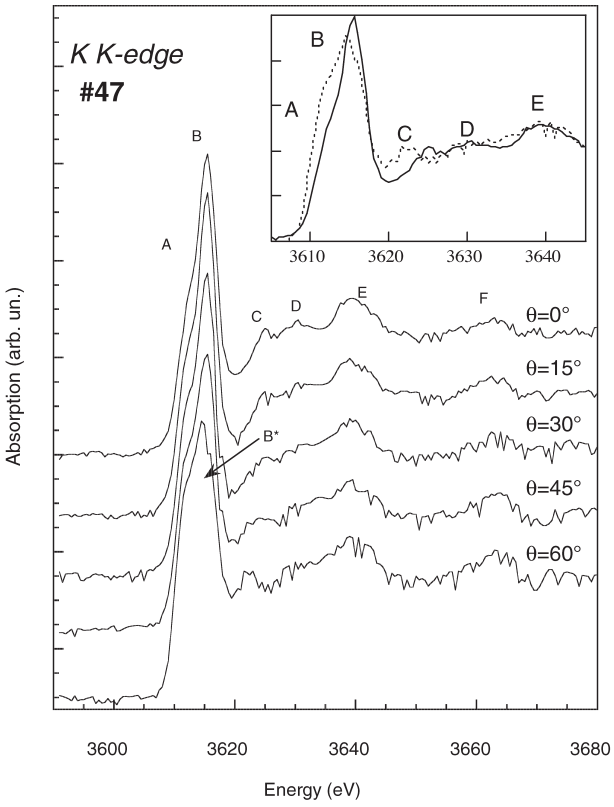

FIGURE 4. Angle-dependent K *K*-XANES spectra recorded on lithian fluorosiderophyllite no. 47 (Lake George ring complex, Pikes Peak, Colorado, U.S.A.) at various θ angles (inset: enlargement of the FMS to IMS section for two extreme rotations).

broader, and (as in Fig. 3) there is indication for the formation of a new feature (B*) as a shoulder on the high-energy limb of edge-top B (Fig. 4, inset). This new feature is stronger than the corresponding Tas22-1 feature because it is partially overlapped by the edge-top B decreasing upper limb; indeed, it could be there from the very beginning, as B is always skew, even in the spectrum taken at θ = 0°. Most IMS features do not move, but become sensibly broader, thus suggesting a generally greater disorder due to photoelectron interaction for the atom planes from which these features originate. Only feature C undergoes a negative shift so as to enter the dip separating the IMS from the FMS sub-region at θ = 0°. There is no indication of new EXAFS-like oscillations at high angle, but this could be due to the very high background noise.

Figure 5 is shown to document the XAFS angular behavior of another trioctahedral mica that is intermediate in composition along the phlogopite–annite join: Tag15-3 with $Fe_{tot}/\Sigma M$ = 0.21 i.e., a ferroan phlogopite that is lithium-free and may be considered to be typical of most igneous rocks (Brigatti and Guggenheim 2002; Table 1a, n. 39; cf. Rieder et al. 1998). This mica is indeed the most interesting study-case of the entire set. With increasing rotation, the edge-top B intensity progressively decreases, while shoulder A increases so as to change into a resolved peak at 3611.6 eV for θ = 75°. Moreover, at this rotation angle a new, well-resolved peak (B*) appears at 3619.5 eV on the high-energy side of edge-top B. As a matter of fact, a faint indication of such a peak could already be detected, albeit as a very shallow shoulder, in the θ = 30° and 45° spectra. By contrast, features C and D, weak but well resolved in all low-angle spectra, almost disappear in the θ = 75° spectrum (Fig. 5, inset). All spectra, whatever their rotation angle, are very well resolved, with sharp peaks nowhere else to be seen but in the fluorophlogopite end-member, which is chemically very pure indeed (Fig. 2). This suggests that the surface of the cleavage flake used was very flat and step-free, and also that the overall structure is free of defects along both the K interlayer and its facing tetrahedral and octahedral sheets. Nevertheless, rotating the blade also induces substantial shape changes in the Tag15-3 K-XANES spectrum, especially for its FMS sub-region: from an essentially single-edged spectrum dominated by a strong edge-top, as typical for K, it turns into a triplet of features where a very weak edge-top feature is still observed over two satellite features of almost equal height. Such a pattern strongly resembles that observed for Mg in a variety of micas (Tombolini et al. 2003), thus suggesting a reduced coordination of K due to the geometry induced by the polarization, or for a very symmetrical distribution of the NN oxygen atoms in two sets of three (above and below) each one forming a triangle, such as in the octahedral coordination. In the IMS sub-region, feature C decreases in intensity while D moves slightly to lower energy. By contrast, the apparent lack of movement of the other IMS features up to EXAFS oscillations underlines that the most local environment around the K cation is essentially insensitive to rotation.

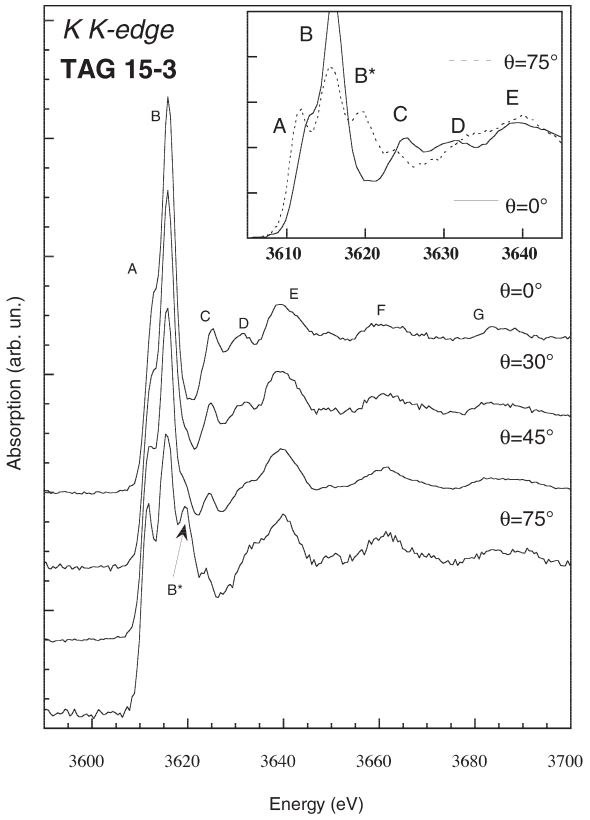

FIGURE 5. Angle-dependent K *K*-XANES spectra recorded on ferroan phlogopite Tag15-3 (Tapira, Minas Gerais, Brazil) at various θ angles (inset: enlargement of the FMS to IMS section for two extreme rotations).

SPECTRUM ANALYSIS

The dependence of XAS spectra on the X-ray beam polarization direction relative to the crystal axes was first noted more than 70 years ago (Cooksey and Stephenson 1933; Stephenson 1933). However, the polarization dependence could not be fully investigated experimentally until the advent of synchrotron radiation. Indeed, it is well known that SR from storage rings is >90% polarized, with the electric vector ε lying in the plane of the ring orbit. Despite the small number of experiments and the difficulty in interpreting results, angle-resolved (viz. polarized) experiments have contributed significantly to our understanding XAFS spectra. Polarized X-rays are particularly useful for transition-metal-bearing compounds at the pre-edge because they may discriminate dipole transitions from the contributions arising by the quadrupolar mechanism (Brümmer et al. 1971; Dräger et al. 1988; Giorgetti et al. 1995; Lang et al. 1995; Heumann et al. 1997; Cabaret et al. 1999). However, until recently, angle-resolved XAFS has not been used extensively in mineral studies, other than to correct the amplitude of EXAFS modulations of self-supporting clay films (Manceau et al. 1998; Manceau and Schlegel 2001). Two conspicuous, scientifically very significant exceptions are the systematics studies at the Fe *K*-edge by Dyar et al. (2001, 2002a). They investigated the extent of XAFS anisotropy in both the pre-edge and the main edge of XANES spectra for several silicates, including trioctahedral mica microcrystals oriented morphologically by the spindle stage (Dyar et al. 2002b). In point of fact, the purpose of their studies was optimization of the XAFS method for quantitative determination of the $Fe^{3+}/\Sigma Fe$ ratio in minerals (Bajt et al. 1994)

as an alternative to the widespread Mössbauer method.

The theory of XANES angular dependence, initially worked out by Izraileva (1966, 1969) in general terms, has been extensively reworked by Brouder (1990) and refined specifically for the three different cases of isotropy, dichroism, and trichroism, so as to become self-consistent. Initially, Brouder (1990, p. 710) used the general dipole absorption cross section approximation, to show that the following formula is valid over the entire energy range that can be investigated by XAFS (i.e., XANES + EXAFS):

$$\sigma^D(\varepsilon) = \sigma^D(0,0) - \sqrt{8\pi/5}\ \Sigma_m Y_2^{m*}(\varepsilon)\ \sigma^D(2,m) \quad (1)$$

where $\sigma^D(\varepsilon) = \sigma^D(0,0)$ for an isotropic (cubic) material as well as for a random powder, and $\sqrt{8\pi/5}\ \Sigma_m Y_2^{m*}(\varepsilon)$ (with m ranging from –2 to 2) are the spherical harmonics arising from angular contributions depending on rotations around the θ and φ axes; in fact, $\sigma^D(\varepsilon)$ is both polar- and azimuthal-angle dependent (Izraileva 1969). The $\sigma^D(2,m)$ coefficient is responsible for the tensor components that affect anisotropic structures.

Brouder (1990 p. 711) subsequently approached the case of dichroism. He stated that it applies to dimetric structures and to all structures developed on two dimensions only, provided they have a ≥3 rotation symmetry. This is indeed the case of the mica layers. Thus they can be assumed to approach a pseudo-hexagonal symmetry, despite the fact that the mica overall structure is monoclinic with space groups for which trichroic formulae are more appropriate: cf. Brouder 1990, Table 5). For dichroic structures the above formula (1) simplifies to:

$$\sigma^D(\varepsilon) = \sigma^D(0,0) - (1/\sqrt{2})\ (3\cos^2\theta - 1)\ \sigma^D(2,0) \quad (2)$$

where θ is the angle between the rotation axis and the polarization vector (Fig. 1). This formula can be rewritten using two components, respectively parallel (in-plane, $\sigma_{\parallel}$) and orthogonal (out-of-plane, $\sigma_{\perp}$) to a reference atomic plane, which is (001) i.e., the cleavage plane in the case of the micas:

$$\sigma_D(\varepsilon) = \sigma_{\parallel} \sin^2\theta + \sigma_{\perp} \cos^2\theta \quad (3)$$

At energies where $\sigma^D(2,0) = 0$, the spectrum is independent of the beam polarization direction. Pettifer et al. (1990) made use of this property to define a "magic angle" theorem. At this angular set up of the sample-holder ($\theta_m = 35.26°$), experimental spectra recorded on powders are representative of the full absorption pattern because they are independent on both polarization and orientation, regardless of whether the powders are randomly or well-oriented (Manceau et al. 1998, p. 350).

Starting from this theoretical background, we extracted the out-of-plane ($\sigma_{\perp}$) and in-plane ($\sigma_{\parallel}$) components from our experimental spectra, using a simple algorithm that first fits the angle dependence for every experimental point on the basis of formula (2) above, using both σ_0 and σ_2 as fitting parameters (Fig. 6). Then, the algorithm reconstructs the individual spectra as a function of every possible rotation angle, including extrapolation to $\theta = 90°$ ($\sigma_{\perp}$) and $\theta = 0°$ ($\sigma_{\parallel}$) as well as to $\theta = 35.26°$ (θ_m). In this way we can directly compare the calculated values to those actually recorded with the mica blade in the starting position and at the magic angle setting. The latter step further aims at comparing the results obtained for mica single crystals to those recorded on the corresponding powders (Cibin et al. 2005). A computer code based on the same algorithm can then back calculate the spectra for any rotation angle, thus allowing a check on all experimental spectra for consistency. Figure 6 shows the end results of the entire extraction procedure for sample phl-Fr, confirming the correctness of our mathematical procedure for all other mica spectra.

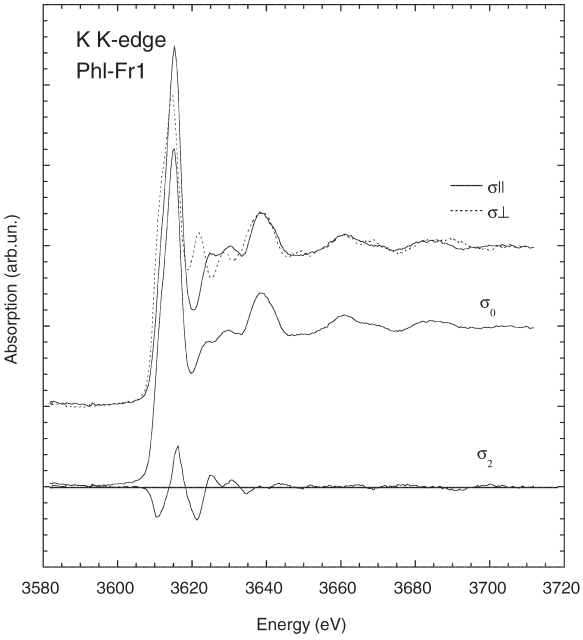

FIGURE 6. Extraction of the components from the potassium *K*-XANES spectrum of fluorophlogopite phl-Fr: (**bottom spectra**) Extraction of σ_2 and σ_0 (isotropic spectrum, matching that of a random powder recorded at the "magic angle") and relative difference spectrum; (**top spectra**) extrapolation of the recorded spectra to $\theta = 90°$ so as to obtain the $\sigma_{\perp}$ (out-of-plane) spectrum, the $\sigma_{\parallel}$ (in-plane) spectrum being the same as σ_2.

Figure 7 shows the complete angular resolved XAFS behavior for another example: intermediate mica Tag15-3, the mica showing the oddest spectral variations on rotation. For this mica, calculations were performed at several, regularly increasing angles. The plotted points are those calculated using equation (2), whereas the continuous lines are the experimental results (Fig. 5). Their overlap supports the results of our calculation, as well as the appropriateness of using only two terms to fit the angular dependence of the mica XANES spectra. Indeed, a two-term fit explains over 90% of the measured signal. The very small residuals shown at the bottom of Figure 7 demonstrate the accuracy of the method to be ca. 3% of the normalized intensity. Far above the edge, the maximum amplitude of the residual signal (0.06 in normalized intensity units) is one order of magnitude smaller than the measured dichroic signal (0.4) in the same energy range, i.e., within the error bar when the same normalized units are used. There is only an anomalously high residual at 3680 eV, but this is present in all samples because it is due to an uncompensated glitch of the monochromator InSb crystal. Close

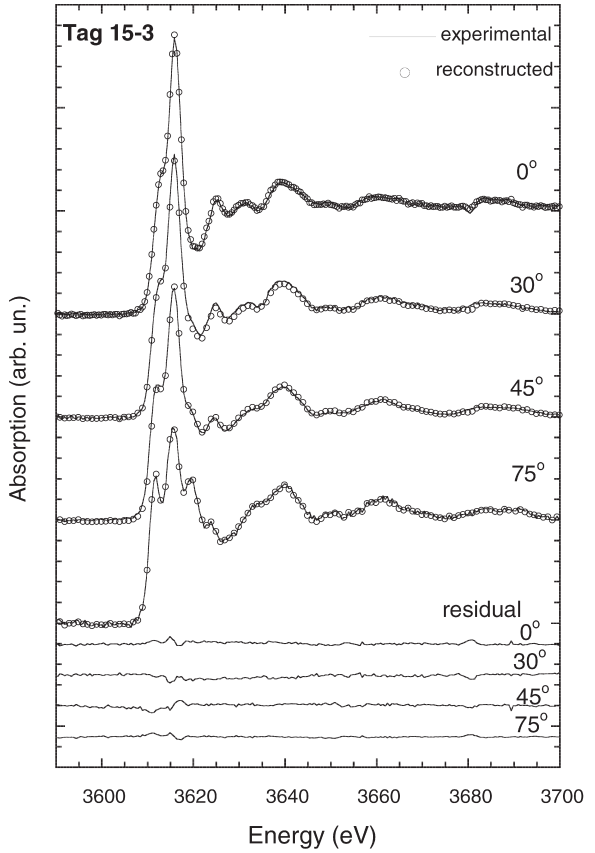

FIGURE 7. Full reconstruction of the Tag15-3 spectra at various θ angles using the σ_2 and σ_0 components extracted according to the formulae listed in text.

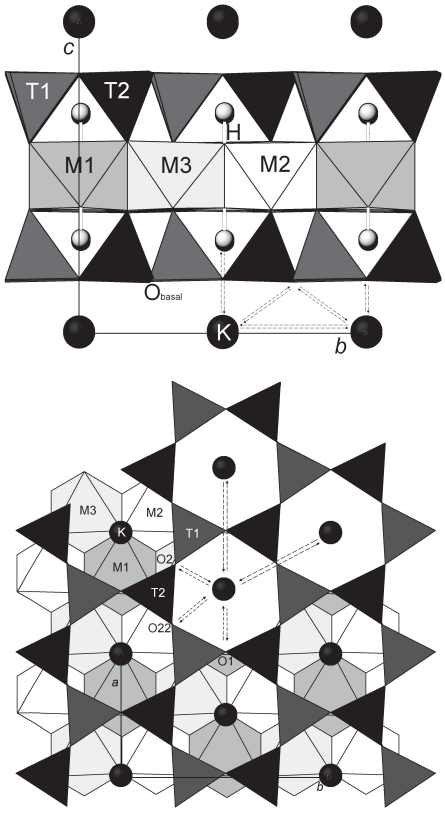

FIGURE 8. Idealized trioctahedral mica crystal structure outlining the multiple-scattering pathways of the photoelectron ejected by a potassium atom located in the interlayer: (**a**) view on the **b-c** plane; (**b**) view on the **a-b** plane, which is parallel to the cleavage surface used when recording the spectra (cf. Fig. 1).

to the edge, the agreement increases to ca. 7% of the measured intensity (within 3σ). However, there are some notable differences, which we interpret as evidence of electronic contributions that superimpose those related to the structure (Marcelli et al. 2000). Furthermore, in this energy region a certain amount of residual may derive from instrumental problems inherent in the TEY detection method (see above).

Concluding, the observed residuals are considered to be compatible with the application of a two-component fitting according to the theoretical approach of Brouder (1990). Although simplified, such a fit appears to satisfy the needs for the angle-dependent absorption behavior of minerals such as trioctahedral micas. Introducing additional fitting parameters may be justified only if a higher-quality detection method is used, such as two-dimensional angle-scanning acquisitions.

DISCUSSION

Figure 8 schematically depicts the mica structure as determined by SC-XRD, respectively on a section **b-c**, i.e., orthogonal (Fig. 8a) and **a-b**, i.e., parallel (Fig. 8b) to the K atoms plane. A photoelectron ejected from the K absorber would interact only with the atoms lying within its fifth/sixth coordination sphere (e.g., Marcelli et al. 2000; Cardelli et al. 2003; Wu et al. 2003, 2005) i.e., with atoms ca. 0.6–0.7 nm away from the absorber (cf. Table 2). Thus, Figure 8 is too schematic, in that it represents the *T* and *M* coordination polyhedra projected on two planes only; actually, the interactions occur three-dimensionally over an entire volume, at both short and medium distances (viz. short- and long-range).

The in-plane ($\sigma_{\parallel}$) component patterns extracted from the experimental XANES spectra of our trioctahedral micas are compared in Figure 9a. As a first approximation, this figure is easy to interpret, both per se with reference to Figure 8b, and by comparison with the powder K *K*-edge spectra of the same micas studied by Cibin et al. (2005; their Figs. 4 and 5). Features A and B in the FMS sub-region were observed in the above study, and are confirmed here, to be essentially constant in energy and shape as they merely reflect the interactions among the K atoms, which are ordered over the *I* interlayer, and the anions around each one of them. Indeed, ECoN is equal to $6 \pm (1 \leq n \leq 6)$ i.e., 6 oxygen atoms plus a variable amount of other oxygen atoms depending on the tetrahedral rotation (Cibin et al. 2005). Most likely, the edge-top B feature originates from interactions of the photoelectron ejected from the K atom with not only its 6 surrounding K NN arranged at the corners of a slightly distorted hexagon (Fig. 8b), but also with its other 6 NN, i.e., the inner bridging O atoms [$O_{b(inner)}$] of the nearest facing *T* sheets across it (Fig. 8a). These $O_{b(inner)}$ are three on each side, the shortest <*A*-O> bonds being,

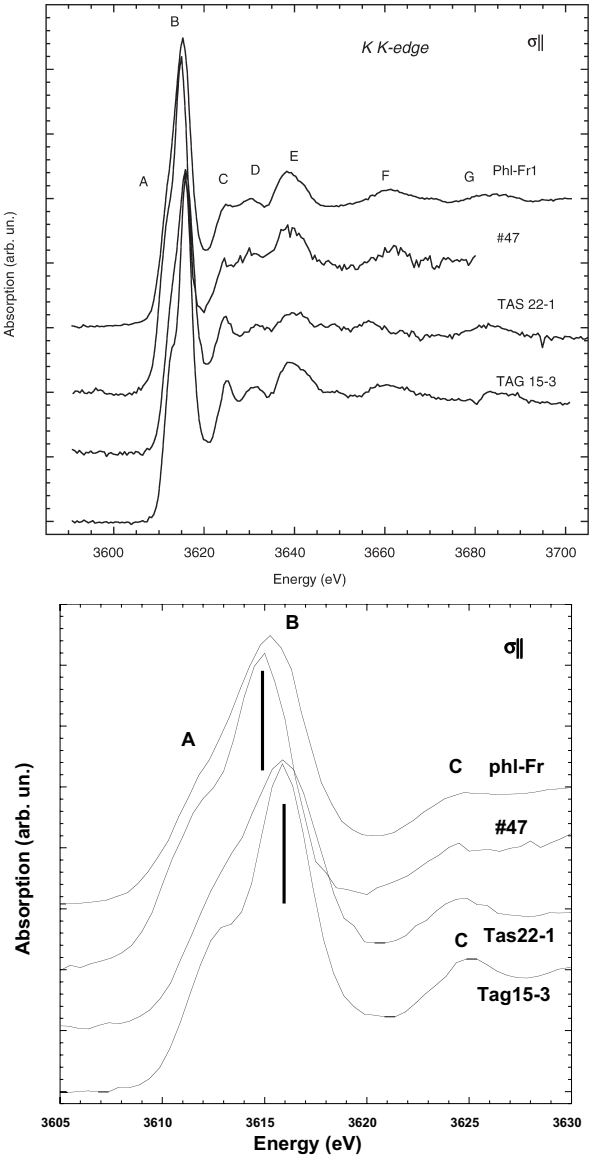

FIGURE 9. In-plane ($\sigma_{\parallel}$) component spectra of the examined micas: (**a**) whole pattern; (**b**) magnification of the 3605–3630 eV energy range. See text for interpretation.

on average, ca. 3.00 Å (Table 2). On the other hand, shoulder A originates from similar photoelectron interactions, in particular with the 6 NNN, i.e., the outer O atoms [$O_{b(outer)}$] of the *T* sheets at ca. 3.33 Å distance. This interpretation is consistent with simulations by the CONTINUUM computer code (Natoli et al. 2003) for mica sample Tas22-1 (Ziyu Wu, personal communication). Calculations for the remaining samples are in progress. The notable small differences in energy in the FMS sub-regions of our four reference micas would appear to merely reflect their small variations in interlayer spacing, a geometrical situation that is bound to be modified by sample rotation. Results similar to those here detected in the calculated in-plane patterns are likely to be found also in the experimental patterns of layer silicates where crystallites are deposited on films so as to lie on one plane only

TABLE 3. Energy positions (eV, ±0.3 eV, except where otherwise indicated) of *K*-XANES features extracted in trioctahedral micas for the two extreme extrapolated rotation angles

Feature	phl-Fr	no. 47	Tas22-1	Tag15-3
		θ = 0°		
E_0	3609.3	3610.0	3611.4	3611.3
A	3611.9	3612.2	3612.2	3612.9
B	3615.3	3615.3	3615.8	3615.9
C	3624.7	3625.0	3624.8	3624.6
D	3630.3	3630.4	3631±1	3631.8
E	3638.4	3639.3	3639.1	3640.1
F	3661±1	3663.5±1	3657±1	3660±1
G	3684±1			3683±1
		θ = 90°		
E_0	3609.8	3609.8	3610.3	3610.2
A	3611.5	3611.0	3612.2	3611.7
B	3614.5	3614.3	3615.7	3615.6
B*			3619.4	3619.3
C	3621.9	3621.6	3624 ± 1	3623.7
D	3628.7	3631 ± 1	3633 ± 1	
E	3638.9		3640.3 ± 1	3634.3
				3639.9
F	3660.7		3649 ± 1	3650.5
	3668.1		3659±1	3661.5
G	3684 ± 1			3683.1
	3689 ± 1			3691.1

(e.g., Manceau et al. 1999; Manceau and Schlegel 2001).

The IMS sub-regions of the four micas display differences in shape combined with significant energy shifts, although they all show the same number of features. The most conspicuous shifts concern features C and E with respect to edge-top B. The former shift (C-B: ca. 2 eV on average; Table 3) was previously shown to be directly related to parameter α, i.e., tetrahedral rotation; indeed, in the mica powder XANES spectra, C-B was found to decrease linearly with α decreasing and with increasing $Fe_{tot}/\Sigma M$ (Cibin et al. 2005; their Fig. 6). Thus, C shifts reflect the adaptation of the tetrahedral sheets to the enlargement of the octahedral sheets due to the replacement of Mg^{2+} by Fe^{2+} in the *M* sites and, in addition but to a lesser extent, of Fe^{3+} substituting for Al in the *T* sites. The same explanation may account for the increasingly stronger negative shifts shown by features E and F, but these features are difficult to measure because of broadening. However, we point out here that our mica spectra appear to be distributed in two pairs: the IMS sub-regions of phl-Fr and no. 47 are very similar, as are those of Tas22-1 and Tag15-3. In these latter spectra there is a notable additional feature located between E and F that is not present in the former pair.

Figure 9b shows the 3605–3635 eV energy ranges of our $\sigma_{\parallel}$ patterns magnified to the maximum allowed by experimental resolution. Under such a much closer observation, they show other significant differences that had previously passed undetected. In particular, phl-Fr and no. 47, on one hand, and Tas22-1 and Tag15-3, on the other hand, are now to be associated in terms of edge feature energy. The former pair has the B edge-top feature at an energy by as much as 1.0 eV lower than the latter one, and it is also significantly broader in shape (FWHM = ca. 3 vs. 2 eV). It is proper to infer that the difference derives from their different anionic surroundings, and has nothing to do with the ordering of K atoms in the interlayer, which is always the same (Table 2). Lower absorption energy implies a lesser binding energy, such as that of the photoelectron ejected by K interacting with the F^- anion located at the O4 site on top of the octahedral

sheet, whereas a sharper shape implies interaction with OH^- in the same site. Here the proton H^+ projects above the octahedral sheet surface, where the O^{2-} lies, toward the open cavity formed below the O_b bridging O atoms of the tetrahedral sheet (Fig. 8a). The different local atomic structures induce a different local and partial density of states (DOS) around the potassium absorber. Actually, the edge features of the XANES spectra reflect the local and partial empty DOS of the absorber atom (Bianconi 1988) and this is to be clearly seen in our micas (Fig. 9b): indeed, phl-Fr and no. 47 are fluoromicas, whereas Tas22-1 and Tag15-3 are not (Table 1). Furthermore, such greater absorption energy is consistent with the presence of a hydrogen bond directed toward the cavity. If this interpretation is correct, the intensity of shoulder A might also be related to the amount of O4 oxygen atoms in the octahedral sheet available for interaction, if any. As a matter of fact, Tag15-3, the mica having the most intense A peak, is also the mica having the largest amount of oxy-substitution i.e., of oxygen in *W* as it results, indirectly, from its high Ti and Fe^{3+} octohedral contents (cf. Table 1). This interpretation further supports our previous conclusion that the A and B features result from and reflect the interlayer K atom ECoN: the B edge-top receives contributions not only from coplanar K atoms ca. 5 Å away (Table 2), but also from photoelectron interactions with the six nearest O atoms, $O_{b(inner)}$. The A feature, correspondingly, is due to interactions with the six more distant $O_{b(outer)}$ O atoms plus the two *W* anions located on top of the octahedral sheet, at ca. 4 Å distance. Consequently, ECoN for K is at least 6 in all micas, plus an additional amount deriving first from the inner bridging O atoms, and second from the outer binding O atoms and possibly from the O4 site. This fraction becomes significant when fluoro- or oxy-substitutions in *W* reduce the amount of protons protruding from the OH^- groups. This deficiency of protons has to be compensated by a different electronic distribution around K, i.e., by different electron DOS.

Summarizing, the $\sigma_{\parallel}$ (in-plane) component in the XANES spectrum points out only structural changes occurring all along the *I* plane (ordered distribution of the K atoms, although with some allowance for the interfering effect of the coexisting minor Na atoms, if any) and its two directly neighboring oxygen planes of the tetrahedral sheet i.e., within the mica interlayer taken as a whole. In special cases (fluoro- and oxy-substituted micas) it appears also to reflect the influence by *W* anions located in the O4 site of the octahedral sheet. It is difficult to determine whether the observed feature intensities are contributed by focusing effects (Kuzmin and Parent 1994), as it would be expected because of the very large number of collinear K atoms involved, or, alternatively, they are not enhanced because they are blurred somewhat by the presence of flattened tetrahedra (parameter τ) and corrugation of the tetrahedral basal oxygen plane (parameter Δz). Both these deformations from ideal geometry are required, together with a reduction of α rotation parameter, to better fit the tetrahedral sheet to an octahedral sheet containing an increased number of large Fe-centered octahedra. As a matter of fact such corrugation of the tetrahedral sheet should appear more clearly in the $\sigma_{\perp}$ spectrum.

Unfortunately, Figure 10, depicting the overall behavior of the $\sigma_{\perp}$ (out-of-plane) component to the XANES spectra of our micas, is more complex to interpret than Figure 9, the more so as background noise in certain spectra hinders examination of, particularly, the IMS sub-regions. Needless to say, the greater number of extracted features by itself underlines the greater complexity of the photoelectron interactions (cf. Figs. 8a, 8b), to a point that practically all four micas differ in their out-of-plane patterns, owing to peculiarities detected either in their IMS or FMS sub-regions. The most important evidence worth discussing concerns the initial sector of the IMS sub-region, where the phl-Fr and no. 47 mica pair apparently shows three well resolved features (C, D, E: Fig. 10a, top pattern), and the Tas22-1 al Tag15-3 pair only two, since C almost disappears under the newly developed feature B*. This should be interpreted in the sense that rotation enhances MS pathways having different orientation and degrees of local order.

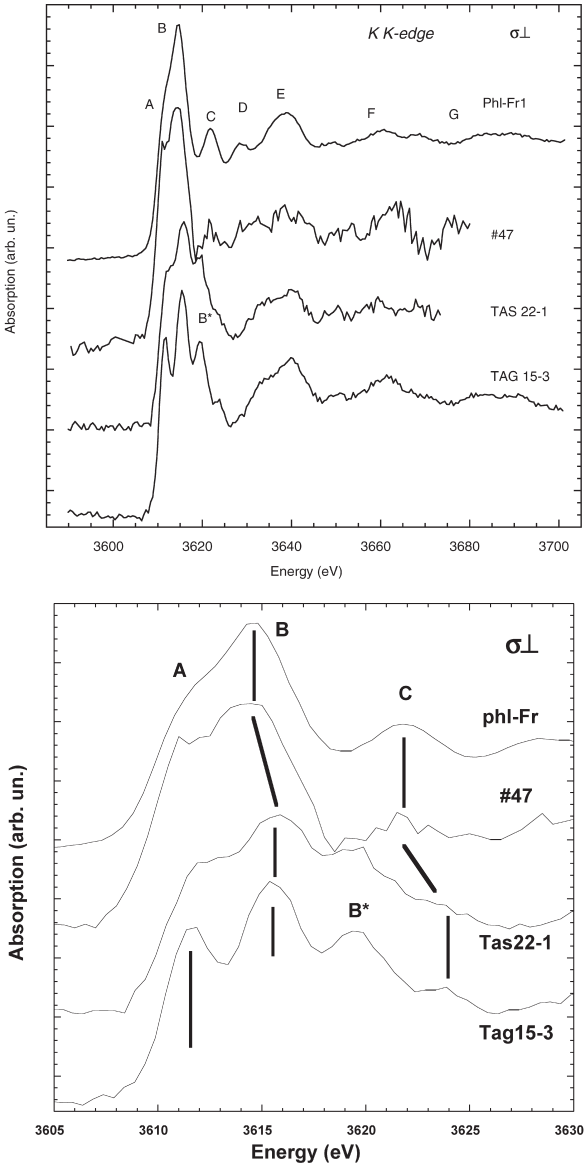

FIGURE 10. Out-of-plane ($\sigma_{\perp}$) component spectra of the examined micas: (**a**) whole pattern; (**b**) magnification of the 3605–3630 eV energy range. See text for interpretation.

From SC-XRD refinements we know that the coordination polyhedron around the K atom is asymmetrical, owing to the monoclinic deformation (β ca. 100°) inherent in the mica structure. This is irrelevant for the in-plane spectra, as most if not all transitions take place alongside the interlayer, which is structurally always the same despite the different widths shown by our four micas (Table 2). By contrast, monoclinic deformation (not shown in the **b**-**c** projection of Fig. 8a, but easy to figure out) causes important modifications in the $\sigma_{\perp}$ (out-of-plane) component spectra. On the whole, such modifications appear to be minor for the phl-Fr and no. 47 mica pair, but become exceedingly significant for Tas22-1 and, particularly, Tag15-3 (Fig. 10a). Indeed, despite the noise, the phl-Fr and no. 47 mica FMS sub-regions are very similar, and are consistent with the polarized Fe-XANES spectra recorded by Dyar et al. (2002b; their Fig. 5) for the Z and Y axes of their Maine phlogopite and Pikes Peak annite i.e., for two micas very similar to those we measured and for two crystallographic directions lying within the **a**-**b** plane. This finding implies that two vastly different cations may show similar absorption behaviors despite their different effective coordinations [6 for Fe, and $6 \pm (1 \leq n \leq 6)$ for K]. As a matter of fact, a reasonable inference is that our phlogopite and lithian siderophyllite should display differences in their K-XANES spectra that reflect only the type of octahedral cation. Indeed, this is the case (cf. Figs. 2 and 4): all observed features are the same, but for the noise, which is greater—obviously—in the latter spectrum. This evidence makes it also reasonable to infer that the photoelectron ejected by the K absorber, after crossing the barrier represented by the tetrahedral sheet, interacts with the heavy atoms (namely with Fe, mostly) located in the octahedral sheet, over 5 Å away, before returning to the absorber through a sequence of MS pathways. In case of an ordered distribution in the octahedral sheet, the effects on the edge region should be magnified.

If this inference is correct, then the Tas22-1 and Tag15-3 spectra, although more complex than the phl-Fr and no. 47 spectra, should be consistent with the Fe-XANES spectra reported by Dyar et al. (2002a). However, this is not easy to see at the first glance in the complete out-of-plane component patterns extracted from the experimental spectra (Fig. 10a), and it shows up only when the extracted patterns are magnified to the maximum extent allowed by experimental resolution (see below). In the spectra as a whole, the most conspicuous difference lies in the energy range between features B and C. Here, in addition to significant energy shifts involving C (also applies to D at higher energy, but to a lesser extent), both the Tas22-1 and Tag15-3 spectra show the formation of a new feature B*, which certainly indicates different and longer MS pathways (probably to highly ordered outer shells with respect to the K absorber). They are different in the above two micas, and need to be investigated and interpreted.

The magnified patterns (Fig. 10b) confirm the significant difference in absorption behavior of pair phl-Fr and no. 47, on one hand, and Tas22-1 and Tag15-3, on the other hand. There is a noticeable difference in edge-top B absorption energy (ca. 1.5 eV), which goes hand in hand with a greater A to B energy difference (ca. 5 eV) and with marked changes in shape of the A feature. Furthermore, as previously mentioned, a feature B* grows on the upper energy limb of B and goes hand in hand with an apparent decrease in intensity of peak C. Peak C also shifts slightly to higher energy values (Table 3).

The explanation of the $\sigma_{\perp}$ component pattern behavior must lie in MS interactions of the photoelectron ejected by K with atoms across the *I* interlayer and the nearby tetrahedral sheets, reaching as far as the interior of the octahedral sheet. Actually, most effects are due to changes in the atom content and distribution within this sheet.

First of all, the distinction of our micas in the same two pairs (see above) based on the B edge-top energies is confirmed. We underline the significant shifts of the E_0 energies toward lower values that occur in all $\sigma_{\perp}$ patterns with respect to those of $\sigma_{\parallel}$ ones (Table 3). This implies a significant change of the empty DOS along the perpendicular direction. The effect is certainly related to the presence of Fe atoms and it is likely to be enhanced by their ordered distribution in the octahedral sheet.

Second, entering further into details (Fig. 10b), we note the following:

(1) The phl-Fr well-structured, sharp $\sigma_{\perp}$ component pattern reflects the highly ordered cation distribution of this mica for both the octahedral sheet, consisting almost entirely of Mg surrounded by O + F, and the tetrahedral sheet, consisting of Si + Al atoms in a ratio close to 3:1 (Table 1).

(2) The no. 47 lithian siderophyllite very noisy $\sigma_{\perp}$ component pattern (although similar to the phl-Fr pattern) reflects the highly disordered structure of the octahedral sheet of this mica. Indeed, this sheet consists of three independent *M* sites, two of them (*M*1 and *M*3) mainly centered by Fe^{2+}, albeit in different amounts, and the third one (*M*2) by the small cation Al (Brigatti et al. 2000, Table 7a). The small cation Li apparently partitions into the *M*1 and *M*3 sites too, thus contributing to the disorder of the octahedral sheet. Mica no. 47 is indeed peculiar: its octahedral parameters are the smallest ones determined in a set of 17 samples from the Pikes Peak complex (Brigatti et al. 2000, Table 5), and its out-of-plane pattern appears to be expanded when compared to that of phl-Fr, thus making it the extreme member of an order-disorder transition leading from lithian micas with *C*12(1) layer symmetry to Li-poor micas with *C*12/*m*(1) layer symmetry (Brigatti et al. 2000; their Fig. 4). The resolved and intense feature A of this mica depends on its electronic properties, and we tentatively suggest that it may originate from long-range interactions with Fe in the octahedral sheet. The large bump that follows A at ca. 3612 eV may also reflect interactions with any one of the two other *M* sites filled by Fe and Li in different amounts, with the overall background noise being clearly related to the total high Fe content of the sample (Table 1).

(3) The well-resolved first feature (labeled A) in the Tas22-1+Tag15-3 pair is at the same energy as the above-mentioned small bump, and as such confirms its assignment to interactions with one of the two independent *M* sites occurring in a normal octahedral sheet i.e., a sheet where $M1 \neq M2 = M3$. As a matter of fact, its intensity probably reflects interactions of the photoelectron with the H proton protruding from the octahedral sheet toward the tetrahedral cavity.

(4) The new feature B* is puzzling. Its intensity and sharpness decrease from Tag15-3 to Tas22-1, thus it cannot be related to photoelectron interactions with Fe^{3+} substituting for Al in the tetrahedral sheet (cf. Table 1). Possibly, it may be related

to clustering of Fe^{3+} cations, but in this case such clustering should occur in both the tetrahedral (Tas22-1) and octahedral sheets (Tag15-3).

(5) By contrast, the decrease in intensity and sharpness of the C feature, which does not move in energy in the first pair and shifts to higher energies in the second pair, where it becomes exceedingly weak, may suggest contributions arising from random MS interactions with Fe^{2+} and Fe^{3+} cations disordered over the octahedral sheet.

Summarizing, the $\sigma_\perp$ (out-of-plane) components of our four mica XANES spectra differ more in their FMS than in their IMS sub-regions, thus suggesting that they certainly reflect electronic interactions, but also structural interactions of the photoelectron with very distant atoms. Actually, both phenomena combine, if one takes for granted that the MS pathways of the photoelectron ejected from the K atom reach as far as the octahedral sheet, so that the photoelectron interacts with the heavy Fe atoms present there. Thus, it seems that the difference in shape and energy of the $\sigma_\perp$ component patterns mainly depends on the different number of Fe^{2+} and Fe^{3+} cations encountered by the photoelectron and on their ordered distribution viz. clustering along the octahedral sheet.

ACKNOWLEDGMENTS

Our research on micas enjoys the joint support of Italy's Ministero dell'Istruzione Universita' e Ricerca (MIUR) and Universita' degli Studi Roma Tre under COFIN 2002 project "Site local order and iron oxidation determination in tri-octahedral micas by XAS." Spectra were recorded at Stanford Synchrotron Radiation Laboratory (SSRL), a facility operated by Stanford University, and supported by the U.S. Department of Energy (DOE), Office of Basic Energy Sciences, and by the Natural Institute of Health (NIH), Biotechnology Resource Program, Division of Research Resources. We thank the SSRL staff, particularly H. Tompkins and C. Troxel, for technical assistance, and G. Giuli, A. Cardelli, and F. Tombolini for sharing time with us while recording spectra. Thanks are due to A. Soldatov (Rostov State University) for making seminal Russian references available. At Istituto Nazionale di Fisica Nucleare (INFN), various staff members of the Laboratori Nazionali di Frascati (LNF) were the source of important theoretical information, and A. Grilli and A. Raco contributed with their technical skill. At Universita' Roma Tre, N. Kreidie and F. De Grisogono assisted in processing the experimental spectra. Two unknown referees, Associate Editor M. Darby Dyar and Editor George A. Lager contributed greatly to increase quality and readability of the manuscript.

REFERENCES CITED

Backhaus, K.-O. and Ďurovič, S. (1984) Polytypism of micas. I. MDO polytypes and their derivation. Clays and Clay Minerals, 32, 453–463.

Bajt, S., Sutton, S.R., and Delaney, J.S. (1994) Microanalysis of iron oxidation states in silicates and oxides using X-ray absorption near edge structure (XANES). Geochimica et Cosmochimica Acta, 58, 5209–5214.

Belov, N.V. (1949) The twin laws of micas and micaceous minerals. Mineralogičeski Sbornik L'vovskoho Geločeskoho Obšestva, 3, 29–40 (in Russian).

Benfatto, M., Natoli, C.R., Bianconi, A., Garcia, J., Marcelli, A., Fanfoni, M., and Davoli, I. (1986) Multiple-scattering regime and higher correlations in X-ray-absorption spectra of liquid solutions. Physical Review, B34, 5774–5781.

Benfatto, M., Congiu Castellano, A., Daniele, A., and Della Longa, S. (2001) MXAN: A new software procedure to perform geometrical fitting of experimental XANES spectra. Journal of Synchrotron Radiation, 8, 267–269.

Bianconi, A. (1988) XANES spectroscopy. In D.C. Konigsberger and R. Prins, Eds., X-ray absorption: principles, applications, techniques of EXAFS, SEXAFS and XANES, p. 573–662. Wiley, New York.

Brigatti, M.F. and Guggenheim, S. (2002) Mica crystal chemistry and the influence of pressure, temperature, and solid solution on atomistic models. In A. Mottana, F.P. Sassi, J.B. Thompson, Jr., and S. Guggenheim, Eds., Micas: Crystal chemistry and metamorphic petrology, 46, 1–97. Reviews in Mineralogy and Geochemistry, Mineralogical Society of America, Chantilly, Virginia.

Brigatti, M.F., Medici, L., and Poppi, L. (1996) Refinement of the structure of natural ferriphlogopite. Clays and Clay Minerals, 44, 540–545.

Brigatti, M.F., Lugli, C., Poppi, L., Foord, E.E., and Kile, D.E. (2000) Crystal chemical variations in Li- and Fe-rich micas from Pikes Peak batholith (central Colorado). American Mineralogist, 85, 1275–1286.

Brigatti, M.F., Galli, E., Medici, L., Poppi, L., Cibin, G., Marcelli, A., and Mottana, A. (2001) Chromium-containing muscovite: crystal chemistry and XANES spectroscopy. European Journal of Mineralogy, 13, 377–389.

Brouder, C. (1990) Angular dependence of X-ray absorption spectra. Journal of Physics: Condensed Matter, 2, 701–738.

Brown, G.S., Eisenberger, P., and Schmidt, P. (1977) Extended X-ray absorption fine-structure studies of oriented single crystals. Solid State Communications, 24, 201–203.

Brümmer, O., Dräger, G., and Stärke, W. (1971) On the mechanism of 3d-transitions in *K*-absorption spectra of transition-metal compounds. Journal de Physique, Colloque C4, Supplément 10, Tome 32, 169–171.

Cabaret, D., Joly, Y., Renevier, H., and Natoli, C.R. (1999) Pre-edge structure analysis of Ti *K*-edge polarized X-ray absorption spectra in TiO_2 by full-potential XANES calculations. Journal of Synchrotron Radiation, 6, 258–260.

Cardelli, A., Cibin, G., Benfatto, M., Della Longa, S., Brigatti, M.F., and Marcelli, A. (2003) A crystal-chemical investigation of Cr substitution in muscovite by XANES spectroscopy. Physics and Chemistry of Minerals, 30, 54–58.

Cibin, G., Mottana, A., Marcelli, A., and Brigatti, M.F. (2005) Potassium coordination in trioctahedral micas by *K*-edge XANES spectroscopy. Mineralogy and Petrology, 85, 67–87.

Cooksey, C.D. and Stephenson, S.T. (1933) Secondary absorption and fine structure of X-rays as observed with a double crystal spectrometer. Physical Review, 43, 670–671.

Dräger, G., Frahm, R., Materlik, G., and Brümmer, O. (1988) On the multiplet character of the X-ray transitions in the pre-edge structure of Fe K absorption spectra. Physica Status Solidi, 146, 287–294.

Dyar, M.D., Delaney, J.S., and Sutton, S.R. (2001) Fe-XANES spectra of iron-rich micas. European Journal of Mineralogy, 13, 1079–1098.

Dyar, M.D., Gunter, M.E., Delaney, J.S., Lanzarotti, A., and Sutton, S.R. (2002a) Systematics in the structure and XANES spectra of pyroxenes, amphiboles, and micas as derived from oriented single crystals. Canadian Mineralogist, 40, 1375–1393.

——— (2002b) Use of the spindle stage for orientation of single crystals for microXAS: Isotropy and anisotropy of Fe-XANES spectra. American Mineralogist, 87, 1500–1504.

Eisebitt, S., Böske, T., Rubensson, J.-E., and Eberhardt, W. (1993) Determination of absorption coefficients for concentrated samples by fluorescence detection. Physical Review, B47, 14103–14109.

Ferraris, G. and Ivaldi, G. (2002) Structural features of micas. In A. Mottana, F.P. Sassi, J.B. Thompson, Jr., and S. Guggenheim, Eds., Micas: Crystal chemistry and metamorphic petrology, 46, p. 117–153. Reviews in Mineralogy and Geochemistry, Mineralogical Society of America, Chantilly, Virginia.

Fleet, M.E. (2003) Deer, Howie, and Zussman rock-forming minerals. Vol. 3A: Micas (2nd edition). Geological Society, London. ISBN 1-86239-142-4

Giorgetti, C., Dartyge, E., Brouder, C., Baudelet, F., Meyer, C., Pizzini, S., Fontaine, A., and Galéra, R.-M. (1995) Quadrupolar effect in X-ray magnetic circular dichroism. Physical Review Letters, 75, 3186–3189.

Giuli, G., Paris, E., Wu, Z., Brigatti, M.F., Cibin, G., Mottana, A., and Marcelli, A. (2001) Experimental and theoretical XANES and EXAFS study of tetraferriphlogopite. European Journal of Mineralogy, 6, 1099–1108.

Gomilšek, J.P., Kodre, A., Arčon, I., and Prešeren, R. (2001) *K*-edge X-ray-absorption spectrum of potassium. Physical Review A, 64, 022508-1–5.

Heald, S.M. and Stern, E.A. (1977) Anisotropic X-ray absorption in layered compounds. Physical Review, B16, 5549–5559.

Heumann, G., Dräger, G., and Bocharov, S. (1997) Angular-dependence in the K pre-edge XANES of cubic crystals: The separation of the empty metal e_g and t_{2h} states of NiO and FeO. Journal de Physique, Colloque C2, Supplément III d'avril, 481–483.

Hoppe, R. (1979) Effective coordination numbers (ECoN) and mean fictive ionic radii (MEFIR). Zeitschrift für Kristallographie, 150, 23–52.

Hoppe, R., Voigt, S., Glaum, H., Kissel, J., Müller, H.P., and Bernet, K. (1989) A new route to charge distribution in ionic solids. Journal of Less-common Metals, 156, 105–122.

Hussain, Z., Umbach, E., Shirley, D.A., Stöhr, J., and Feldhaus, J. (1982) Performance and application of a double crystal monochromator in the energy region $800 \le h\nu \le 4500$ eV. Nuclear Instruments and Methods in Physics Research, 195, 115–131.

Izraileva, L.K. (1966) Theory of the high-energy region of X-ray absorption on monocrystal and polycrystalline materials. Doklady Akademia Nauk SSSR, 11, 777–781 (in Russian).

——— (1969) Polarized and unpolarized X-ray absorption by monocrystals. In Anonymous, Ed., X-ray spectra and electronic structure of matter, II, p. 211–221. Instituti Metallofizika Academia Nauk, Kiev (in Russian).

Kasrai, M., Lennard, W.N., Brunner, R.W., Bancroft, G.M., Bardwell, J.A., and Tan, K.H. (1996) Sampling depths of total electron yield and fluorescernce measurements in Si L- and K-edge absorption spectroscopy. Applied Surface Science, 99, 303–312.

Kasrai, M., Fleet, M.E., Muthupari, S., Li, D., and Bancroft, G.M. (1998) Surface modification study of borate materials from B *K*-edge X-ray absorption spec-

troscopy. Physics and Chemistry of Minerals, 25, 268–272.
Kuzmin, A. and Parent, Ph. (1994) Focusing and superfocusing effects in X-ray absorption fine structure at the iron *K* edge in FeF_3. Journal of Physics: Condensed Matter, 6, 4395–4404.
Lang, J.C, Šrajer, G., Detlefs, C., Goldman, A.I., König, H., Wang, X., Harmon, B.N., and McCallum, R.W. (1995) Confirmation of quadrupolar transitions in circular magnetic X-ray dichroism at the Dysprosium L_{III} edge. Physical Review Letters, 74, 4935–4938.
Lavrentyev, A.A., Gabrelian, B.V., Nikiforov, I.Ya., and Rehr, J.J. (1999) Ab initio XANES calculations for KCl and PbS. Journal of Physics and Chemistry of Solids, 60, 787–790.
Lee, H.-L. and Guggenheim, S. (1981) Single crystal refinement of pyrophyllite-1*Tc*. American Mineralogist, 66, 350–357.
Lytle, F.W., Greegor, R.B., Sandstrom, D.R., Marques, E.C., Wong, J., Spiro, C.L., Huffman, G.P., and Huggins, F.E. (1984) Measurement of soft X-ray absorption spectra with a fluorescent ion chamber detector. Nuclear Instruments and Methods in Physics Research, 226, 542–548.
Manceau, A. and Schlegel, M.L. (2001) Texture effect on polarized EXAFS amplitude. Physics and Chemistry of Minerals, 28, 52–56.
Manceau, A., Bonnin, D., Kaiser, R., and Frétigny, C. (1988) Polarized EXAFS of biotite and chlorite. Physics and Chemistry of Minerals, 16, 180–185.
Manceau, A., Bonnin, D., Stone, W.E.E., and Sanz, J. (1990) Distribution of Fe in the octahedral sheet of trioctahedral micas by polarized EXAFS: comparison with NMR results. Physics and Chemistry of Minerals, 17, 363–370.
Manceau, A., Chateigner, D., and Gates, W.P. (1998) Polarized EXAFS, distance-valence least-squares modeling (DVLS), and quantitative texture analysis approaches to the structural refinement of Garfield nontronite. Physics and Chemistry of Minerals, 25, 347–365.
Manceau, A., Schlegel, M.L., Chateigner, D., Lanson, B., Bartoli, C., and Gates, W.P. (1999) Application of polarized EXAFS to fine-grained layered minerals. In D. Schulze, P. Bertsch, and J.W. Stucky, Eds., Synchrotron X-ray methods in clay science, 9, p. 68–114. CMS workshop lecture, Clay Minerals Society, Boulder, Colorado.
Marcelli, A., Mottana, A., and Cibin, G. (2000) Next-near-neighbour interactions with Al in Li^+- and Rb^+-exchanged Na^+ β-aluminas, detected by synchrotron X-ray absorption spectroscopy. Journal of Applied Crystallography, 33, 234–242.
Meyrowitz, R. (1970) A semimicroprocedure for the determination of ferrous iron in nonrefractory silicate minerals. American Mineralogist, 48, 340–347.
Mottana, A. (2004) X-ray absorption spectroscopy in mineralogy: Theory and experiment in the XANES region. In A. Beran and E. Libowitzky, Eds., Spectroscopic methods in mineralogy, 6, p. 465–522. European Mineralogical Union Notes in Mineralogy, Eötvös University Press, Budapest. ISBN 963-463-662-4
Mottana, A., Robert, J.-L., Marcelli, A., Giuli, G., Della Ventura, G., and Paris, E. (1997) Octahedral vs. tetrahedral coordination of Al in synthetic micas determined by XANES. American Mineralogist, 82, 497–502.
Mottana, A., Marcelli, A., Cibin, G., and Dyar, M.D. (2002a) X-ray absorption spectroscopy of the micas. In A. Mottana, F.P. Sassi, J.B. Thompson, Jr. and S. Guggenheim, Eds., Micas: Crystal chemistry and metamorphic petrology, 46, p. 371–412. Reviews in Mineralogy and Geochemistry, Mineralogical Society of America, Chantilly, Virginia.
Mottana, A., Sassi, F.P., Thompson, J.B., Jr., and Guggenheim, S., Eds. (2002b) Micas: Crystal chemistry and metamorphic petrology, 46. Reviews in Mineralogy and Geochemistry, Mineralogical Society of America, Chantilly, Virginia.
Natoli, C.R., Benfatto, M., Della Longa, S., and Hatada, K. (2003) X-ray absorption spectroscopy: state-of-the-art analysis. Journal of Synchrotron Radiation, 10, 26–42.
Nespolo, M. and Ďurovič, S. (2002) Crystallographic basis of polytypism and twinning in micas. In A. Mottana, F.P. Sassi, J.B. Thompson, Jr., and S. Guggenheim, Eds., Micas: Crystal chemistry and metamorphic petrology, 46, p. 155–279. Reviews in Mineralogy and Geochemistry, Mineralogical Society of America, Chantilly, Virginia.
Nespolo, M., Takeda, H., and Ferraris, G. (1997) Crystallography of mica polytypes. In S. Merlino, Ed., Modular aspects of minerals, 1, p. 81–118. European Mineralogical Union Notes in Mineralogy, Eötvös University Press, Budapest. ISBN 963-463-1320
Nespolo, M., Ferraris, G., and Ohashi, H. (1999) Charge distribution as a tool to investigate structural details: Meaning and application to pyroxenes. Acta Crystallographica, B55, 902–916.
Pauling, L. (1930) The structure of micas and related minerals. Proceedings of the National Academy of Science (U.S.A.), 16, 123–129.
Pettifer, R.F., Brouder, C., Benfatto, M., Natoli, C.R., Hermes, C., and Ruiz López, M.F. (1990) Magic-angle theorem in powder X-ray-absorption spectroscopy. Physical Review, B42, 37–42.
Prešeren, R., Kodre, A., Arčon, I., Gomilšek, J.P., and Hribar, M. (1999) A simple heat-pipe cell for X-ray absorption spectrometry of potassium vapor. Nuclear Instruments and Methods in Physics Research, B149, 238–239.
Radoslovich, E.W. (1961) Surface symmetry and cell dimensions of layer-lattice silicates. Nature, 191, 67–68.
Radoslovich, E.W. and Norrish, K. (1962) The cell dimensions and symmetry of layer-lattice silicates. I. Some structural considerations. American Mineralogist, 47, 599–616.
Rieder, M., Cavazzini, G., D□yakonov, Y.S., Frank-Kamenetskii, V.A., Gottardi, G., Guggenheim, S., Koval, P.V., Müller, G., Neiva, A.M.R., Radoslovich, E.W., Robert, J.-L., Sassi, F.P., Takeda, H., Weiss, Z., and Wones, D.R. (1998) Nomenclature of the micas. Clays and Clay Minerals, 41, 61–72.
Smyth, J.R. and Bish, D.L. (1988) Crystal structures and cation sites of rock-forming minerals. Allen and Unwin, Boston. ISBN 0-04-445004-4
Stärke, W., Brümmer, O., Dräger, G., Nikiforov, I.Ya., Sachenko, V.P., and Richter, J. (1972) Application of crystal field theory for interpretation of the Fe *K*- and Cr *K*-edges in their oxides. Izvestia Akademii Nauk CCCP, Serja Fiziceskaja, 36, 219–222 (in Russian).
Stephenson, S.T. (1933) Fine structure in the K X-ray absorption spectrum of bromine. Physical Review, 44, 349–352.
Tombolini, F., Brigatti, M.F., Marcelli, A., Cibin, G., Mottana, A., and Giuli, G. (2002a) Local and average Fe distribution in trioctahedral micas: Analysis of the Fe *K*-edge XANES spectra in the phlogopite-annite and phlogopite-tetraferriphlogopite joins on the basis of single-crystal XRD refinements. European Journal of Mineralogy, 14, 1075–1186.
Tombolini, F., Marcelli, A., Mottana, A., Cibin, G., Brigatti, M.F., and Giuli, G. (2002b) Crystal-chemical study by XANES of trioctahedral micas: the most characteristic layer silicates. International Journal of Modern Physics, B16, 1673–1679.
Tombolini, F.,, Cibin, G., Marcelli, A., Mottana, A., Brigatti, M.F., and Giuli, G. (2003) A polarized XANES investigation of Mg-rich trioctahedral micas. In A. Bianconi, A. Marcelli, and N.L. Saini, Eds., X-Ray and Inner-Shell Processes: 19th International Conference on X-ray and Inner-Shell Processes, 481–490 (American Institute of Physics Conference Proceedings 652). American Institute of Physics, Mineola, New York. ISBN 0-7354-0111-X
Trischka, J.W. (1945) Structure in the X-ray *K* absorption edges of solid potassium chloride. Physical Review, 67, 318–320.
Vedrinskii, R.V., Bugaev, L.A., Gegusin, I.I., Kraizman, V.L., Novakovich, A.A., Prosandeev, S.A., Ruus, R.E., Maiste, A.A., and Elango M.A. (1982) X-ray absorption near edge structure (XANES) for KCl. Solid State Communications, 44, 1401–1407.
Waychunas, G.A. and Brown, G.E., Jr. (1990) Polarized X-ray absorption spectroscopy of metal ions in minerals. Physics and Chemistry of Minerals, 17, 420–430.
Weiss, Z., Rieder, M., and Chmielová, M. (1992) Deformation of coordination polyhedra and their sheets in phyllosilicates. European Journal of Mineralogy, 4, 665–682.
Wu, Z., Marcelli, A., Cibin, G., Mottana, A., and Della Ventura, G. (2003) Investigation of the mica X-ray absorption near-edge structure spectral features at the Al *K*-edge. Journal of Physics: Condensed Matter, 15, 7139–7148.
——— (2005) Aluminium *K*-edge XANES study of mica preiswerkite. Physica Scripta, T115, 172–174.

MANUSCRIPT RECEIVED JULY 21, 2005
MANUSCRIPT ACCEPTED FEBRUARY 27, 2006
MANUSCRIPT HANDLED BY DARBY DYAR